

# Comparative Chronoamperometry: Spheres, Discs, Cylinders and Bands

Haonan Le, and Richard G. Compton<sup>1</sup>

Department of Chemistry, Physical and Theoretical Chemistry Laboratory, Oxford University

South Parks Road, Oxford, OX1 3QZ, United Kingdom

## Abstract

A parameter, the diffusion indicator  $\alpha$ , introduced in this work, is derived from chronoamperometric current responses to obtain comparative information about the diffusion of an electrochemically active species from/to an electrode. The  $\alpha$  values are used to investigate the diffusion to four electrodes with different geometries: microsphere, microdisc, microcylinder, and microband electrodes based on literature analytical and empirical equations for their chronoamperometric currents and the associated concentration profiles extracted from new simulations. The values of  $\alpha$  and their time evolution show the contrasting contribution of planar and convergent/divergent diffusion in the different geometries.

Keywords: Diffusion indicator; Microelectrode; Chronoamperometry; Diffusion

## 1 Introduction

Microelectrodes are universally employed in both fundamental and analytical electrochemistry and take the form of a wide diversity of, usually regular, geometries of which spheres [1–3], discs [4–6], cylinders [7–10], and bands [11–13] are the most common (see **Figure 1**). The several generic advantages of microelectrodes over their macro counterparts are well rehearsed and include the access to shorter timescales,

---

<sup>1</sup> Corresponding author: Richard G. Compton, richard.compton@chem.ox.ac.uk

greater current densities and reduced total interfacial capacitances. The shorter timescales facilitate the measurement of faster kinetics - both heterogeneous and of coupled homogeneous reactions - as perhaps best illustrated by the fast scan (mega-Volt per second) cyclic voltammetry at microdisc electrodes pioneered by Amatore, Maisonhaute and colleagues [14, 15] and where ‘faster’ compares to what is seen at macroelectrodes.

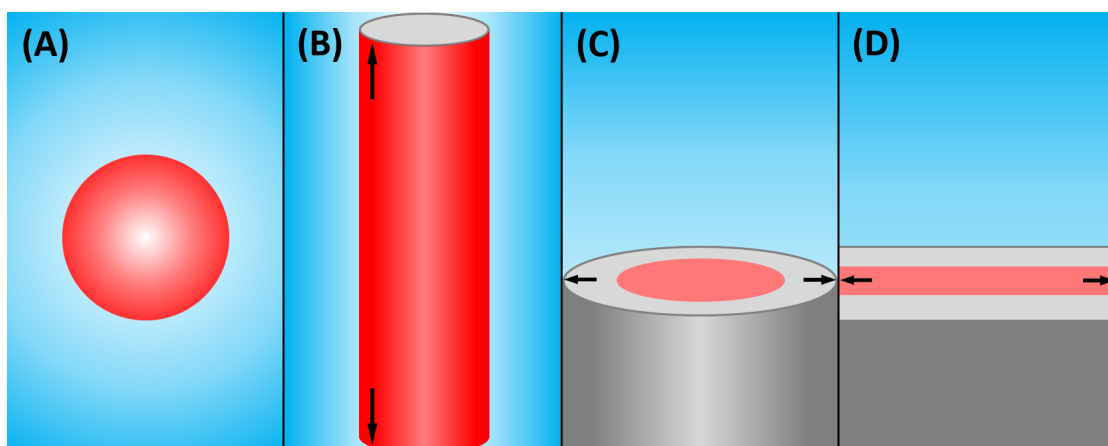


**Figure 1:** Illustrations of the electrodes investigated: **(A)** the microsphere electrode, **(B)** the infinite microcylinder electrode, **(C)** the microdisc electrode, and **(D)** the infinite microband electrode. The red areas indicate the electrochemically active surfaces, the blue areas represent the solution phase, the grey areas represent the insulating surface, and the black arrows represent infinitely expanding areas.

Whilst the four microelectrode geometries shown in **Figure 1** all show faster responses than macroelectrodes, they show interesting differences between themselves. This is especially noticeable in the diffusion-controlled limit of simple Faradaic processes where in the case of a microdisc, or microsphere, electrode a true steady-state limiting current  $I_{ss}$ . In particular, for the reaction  $A \pm ne \rightarrow B$ , the steady-state current for a microdisc electrode is [16, 17]:

$$I_{ssD} = 4r_enFc^*D \quad (1)$$

where  $r_e$  is the radius of the microdisc electrode,  $n$  is the number of electrons transferred in the electrode reaction,  $F$  is the Faraday constant,  $c^*$  is the initial concentration of the

analyte  $A$ , and  $D$  is the diffusion coefficient of  $A$ .

The corresponding equation for a microsphere is [18]:

$$I_{ss} = 4\pi r_e n F c^* D \quad (2)$$

where again a true steady state results from the fully convergent diffusion of  $A$  to the electrode.

In contrast, the Faradaic responses at microcylinder and microband electrodes show only a quasi-steady state behaviour in which an almost constant limiting current decays very slowly ultimately, in principle at least, to zero. There are well-known approximations for the currents following a potential step from zero current to the diffusion-controlled electrolysis of  $A$  which are, for a microcylinder of infinite length and radius  $r_e$  [19],

$$I_{qssc} = \frac{4\pi n F c^* D l}{\ln(4Dt/r_e^2)} \quad (3)$$

and, for an infinitely long microband of width  $w$  [20],

$$I_{qssB} = \frac{2\pi n F c^* D l^*}{\ln(64Dt/w^2)} \quad (4)$$

where  $l$  and  $l^*$  are the lengths of the cylinder and the band, respectively, and  $w$  is the width of the band.

In both cases the decrease of current at long times is evident. The difference in these geometries from these showing true steady-state current and fully convergent diffusion lies in the band and the cylinder possessing one spatial dimension which is macroscopic in scale - the electrode length in each case - and it is this feature which ensures that the current ultimately decays to zero under diffusion-only conditions.

In experimental practice, a key question, other than the issue of steady-state versus quasi-steady-state behaviour, relates to the speed of responses of the electrode to a potential perturbation. In the following we compare and contrast the chronoamperometric responses of the four electrodes of interest to a potential step from

zero- to a diffusion-limited current. As a means of comparing the relative timescales and the evolution of the current responses from a linear, Cottrellian, diffusion, behaviour over to a steady-state or quasi-steady state, we make use of an approach newly introduced in respect of our analysis of different types of cylindrical electrodes [21]. This approach notes that for all the electrodes of interest the short-time behaviour reflects linear diffusion and so the currents scale as:

$$I \propto t^{-0.5} \quad (5)$$

For fully convergent diffusion where a steady state is established,

$$I \propto t^0 \quad (6)$$

Thus, the transition from the limit of linear diffusion to that of convergent or quasi-convergent diffusion in the course of a potential step current-time transient can be characterised by the parameter:

$$\alpha = 2 \frac{d(\log I)}{d(\log t)} + 1 \quad (7)$$

where the two limiting cases form the lower and upper values of  $\alpha$ :  $0 \leq \alpha \leq 1$  such that  $\alpha = 0$  corresponds to linear diffusion and  $\alpha = 1$  to fully convergent diffusion. We have termed the parameter  $\alpha$  the “diffusion indicator” relating to the character of the diffusion.

## 2 Simulation methods

In this section, the simulation models are presented first before, second, the computational methods and dimensionless parameters adopted in this work are introduced.

### 2.1 Simulation models

This work employs four simulation models for the different geometries as shown in the previous section and investigates in their current responses and concentration

profiles for potential step chronoamperometry. The initial concentration of the species  $A$  in each model is set to be  $c^*$  uniformly for all space points before an overpotential is applied to the electrochemically active surface, where a single-electron-transfer reduction occurs for the species  $A$  ( $A + e^- \rightarrow B$ ). The potential step chronoamperometric process in each model is assumed to be diffusion-controlled by setting a large overpotential and sufficiently high concentration of electrolyte. Therefore, the following diffusion equation can be used to describe the mass transport in the reduction process.

$$\frac{\partial y}{\partial x} = D \nabla^2 c \quad (8)$$

where  $c$  is the species concentration at a certain space point, and  $t$  is the time.  $\nabla$  is a vector operator related to the coordinate system chosen.

Due to the similarities in geometries, the models are presented in two groups: first, the microsphere electrode and the microcylinder electrode models, and second, the microdisc electrode and the microband electrode models. The details for each group are introduced separately as follows.

### 2.1.1 Microsphere electrode and microcylinder electrode models

In the microsphere electrode model, due to its rotational symmetry, the model can be simplified to a one-dimensional spherical system. Therefore,  $\nabla^2$  can be simplified, and the diffusion equation of this system is:

$$\frac{\partial c}{\partial t} = D \nabla^2 c = D \left( \frac{\partial^2 c}{\partial r^2} + \frac{2}{r} \frac{\partial c}{\partial r} \right) \quad (9)$$

Similarly, the diffusion equation of the microcylinder model can be simplified to:

$$\frac{\partial c}{\partial t} = D \nabla^2 c = D \left( \frac{\partial^2 c}{\partial r^2} + \frac{1}{r} \frac{\partial c}{\partial r} \right) \quad (10)$$

due to the horizontal symmetry and rotational symmetry in the infinite microcylinder electrode model.

Therefore, the simulation of these two models can be presented as in **Figure 2(A)**, which shows the one-dimensional geometries at an extremely small scale for these two models. The analyte  $A$  in the solution shown at the right side of the plot is illustrated in blue, and the electrode shown at the left is coloured in red, where the single-electron-transfer reduction occurs. The only difference between these two one-dimensional models is the different radial diffusion, which is respectively represented by the terms  $\frac{2}{r} \frac{\partial c}{\partial r}$  and  $\frac{1}{r} \frac{\partial c}{\partial r}$  in **Equations (9)** and **(10)**, during the simulated processes.

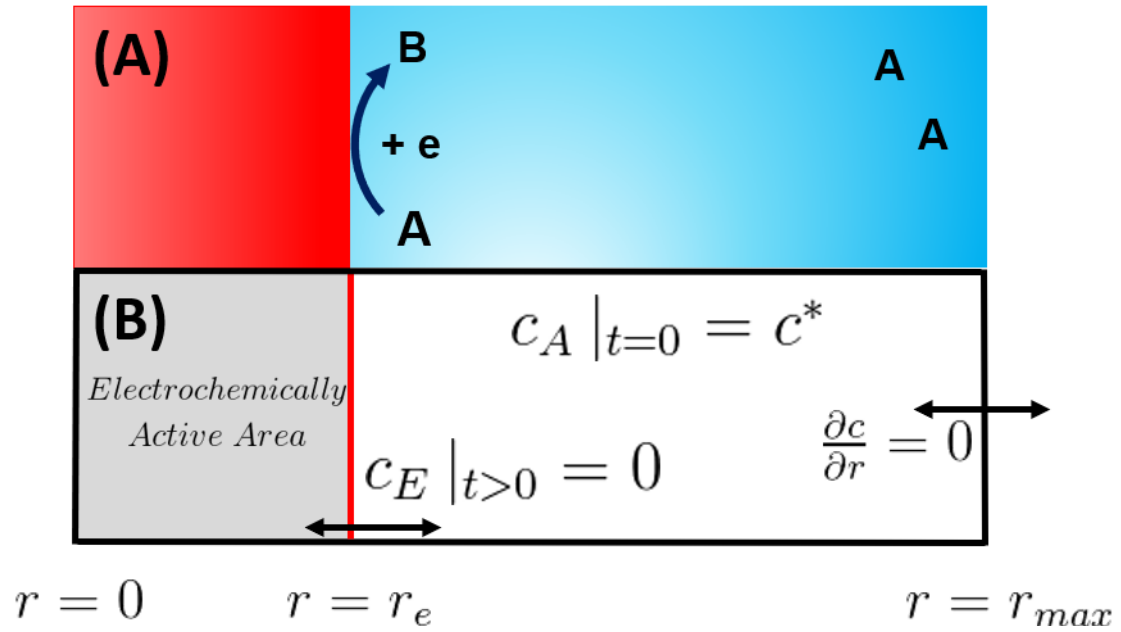


**Figure 2:** Cross-sectional illustration (A) and boundary conditions (B) of the microsphere electrode model and the infinite microcylinder electrode model.  $c_A |_{t=0}$  represents the concentration of the analyte  $A$  for all of the points within the simulated space at the beginning of the simulation,  $c^*$  is the initially homogeneous concentration of the analyte  $A$ ,  $c_E$  is the concentration of the analyte  $A$  for points at the surface of the electrochemically active area,  $r_e$  is the radius of the cylinder, and  $r_{max}$  is the boundary of the simulated space in the  $r$ -axis.

In **Figure 2(B)**, the boundary conditions for these two simulation models are shown with the necessary equations. In detail, the concentration of analyte  $A$  is set to be  $c^*$  with concentration of  $B$  setting to zero:

$$t = 0, \quad r_e \leq r \leq r_{max}: \quad c_A = c_A^*, c_B = 0 \quad (11)$$

where  $r_{max}$  represent the far end of the simulation space away from the electrode, which

is the sum of the electrode radius  $r_e$  and the solution space  $x_{sim}$ :

$$\begin{cases} r_{max} = r_e + x_{sim} \\ x_{sim} = 6\sqrt{Dt_{sim}} \end{cases} \quad (12)$$

where  $t_{sim}$  is the total simulation time. As described in the literature [22, 23], due to Brownian motion, the distance from the electrode for the concentration perturbation to occur is around:  $\sqrt{\langle x \rangle^2} = \sqrt{2Dt_{sim}}$ . Therefore,  $x_{sim}$  is set large enough,  $\sqrt{6Dt_{sim}}$ , that the simulation process is independent of the far end boundary  $r_{max}$ .

After the beginning of each reduction process, a no-flux boundary condition is set at the far end boundary in the simulation while, due to the overpotential applied, the concentration of  $A$  on the electrodes surface ( $r = r_e$ ) is set to zero:

$$\begin{cases} t > 0, & r = r_{max}: & \frac{\partial c}{\partial r} = 0 \\ t > 0, & r = r_e: & c_A = 0 \end{cases} \quad (13)$$

According to Fick's first law and Faraday's law, the current responses in two electrode models in this section as:

$$\begin{cases} I_s = Fj_s & \text{where } j_s = -4\pi r_e^2 D \frac{\partial c_A}{\partial r} \big|_{r=r_e} \\ I_c = Fj_c & \text{where } j_c = -2\pi l r_e D \frac{\partial c_A}{\partial r} \big|_{r=r_e} \end{cases} \quad (14)$$

where  $I_s$  and  $I_c$  are the current responses for the microsphere electrode model and the microcylinder electrode model, respectively,  $j_s$  and  $j_c$  are the fluxes of the analyte  $A$  for the microsphere electrode model and the microcylinder electrode model, respectively.

### 2.1.2 Microdisc electrode model and microband electrode model

Similar to previous model, due to the rotational symmetry, the microdisc electrode model can be simplified to a two-dimensional spherical system, and the diffusion equation of this system is:

$$\frac{\partial c}{\partial t} = D\nabla^2 c = D\left(\frac{\partial^2 c}{\partial r^2} + \frac{1}{r}\frac{\partial c}{\partial r} + \frac{\partial^2 c}{\partial z^2}\right) \quad (15)$$

and the diffusion equation for the microband electrode model can be simplified, according to the vertical symmetry, to:

$$\frac{\partial c}{\partial t} = D \nabla^2 c = D \left( \frac{\partial^2 c}{\partial r^2} + \frac{\partial^2 c}{\partial z^2} \right) \quad (16)$$

as shown in **Figure 3(A)**.

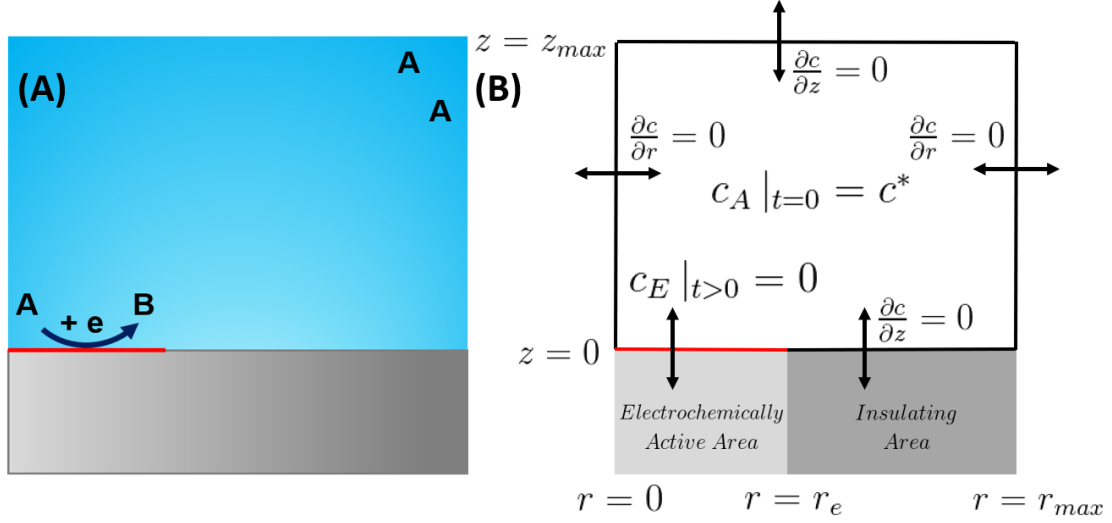


**Figure 3:** Cross-sectional illustration **(A)** and boundary conditions **(B)** of the microdisc electrode model and the microband electrode model.  $z_{max}$  is the boundary of the simulated space in the  $z$ -axis.

As illustrated in **Figure 3(A)**, the boundary conditions for these two models can be set in the same way. Firstly, the concentrations of species  $A$  and  $B$  within the simulation spaces are set to  $c^*$  and zero, respectively, at the beginning of the simulations:

$$t = 0, \quad 0 \leq r \leq r_{max}, \quad 0 \leq z \leq z_{max}: \quad c_A = c^*, c_B = 0 \quad (17)$$

For  $t > 0$ , the concentration of  $A$  for the space points at the electrode surface are set to zero because of the overpotential:

$$t > 0, \quad 0 \leq r \leq r_e, \quad z = 0: \quad c_A = 0 \quad (18)$$

and the rest of the boundaries are set to be no-flux boundaries:

$$\begin{cases} t > 0, \quad r = 0, 0 \leq z \leq z_{max}: & \frac{\partial c}{\partial r} = 0 \\ t > 0, \quad r = r_{max}, 0 \leq z \leq z_{max}: & \frac{\partial c}{\partial r} = 0 \\ t > 0, \quad z = 0, r_e \leq r \leq r_{max}: & \frac{\partial c}{\partial z} = 0 \\ t > 0, \quad z = z_{max}, 0 \leq r \leq r_{max}: & \frac{\partial c}{\partial z} = 0 \end{cases} \quad (19)$$

under similar conditions that the simulation space  $x_{sim}$  is determined by the simulation time:

$$\begin{cases} r_{max} = r_e + x_{sim} \\ z_{max} = x_{sim} \\ x_{sim} = 6\sqrt{Dt_{sim}} \end{cases} \quad (20)$$

Therefore, the current responses can be calculated according to the fluxes of species  $A$  at the electrode surface:

$$\begin{cases} I_D = Fj_D \quad \text{where} \quad j_D = -2\pi D \int_0^{r_e} \frac{\partial c_A}{\partial z} \big|_{z=0} r dr \\ I_B = Fj_B \quad \text{where} \quad j_B = -2l^* D \int_0^{r_e} \frac{\partial c_A}{\partial z} \big|_{z=0} dr \end{cases} \quad (21)$$

## 2.2 Dimensionless parameters

In order to present the simulation and theory results in a simple and universal way, dimensionless parameters are introduced as shown in **Table 1**.

**Table 1:** Transformation of dimensional parameters to dimensionless parameters where  $r_r$  is the reference length of the respective model,  $R$  is the Universal Gas Constant, and  $T$  is the temperature.

Dimensionless Parameter	Conversion
Concentration of species j	$C_j = \frac{c_j}{c^*}$
Diffusion coefficient of species j	$d_j = \frac{D_j}{D}$
Radial distance	$R = \frac{r}{r_r}$
Axial distance	$Z = \frac{z}{r_r}$
Time	$T = \frac{Dt}{r_r^2}$
Potential	$\theta = \frac{F}{RT}(E - E_f^0)$
Current	$J = \frac{I}{Fr_r D c^*}$

Diffusion equations (9), (10), (15), and (16) can be transformed into dimensionless forms:

$$\begin{cases} \frac{\partial C_j}{\partial T} = d_j \left( \frac{\partial^2 C_j}{\partial R^2} + \frac{2}{R} \frac{\partial C_j}{\partial R} \right) \\ \frac{\partial C_j}{\partial T} = d_j \left( \frac{\partial^2 C_j}{\partial R^2} + \frac{1}{R} \frac{\partial C_j}{\partial R} \right) \\ \frac{\partial C_j}{\partial T} = d_j \left( \frac{\partial^2 C_j}{\partial R^2} + \frac{1}{R} \frac{\partial C_j}{\partial R} + \frac{\partial^2 C_j}{\partial Z^2} \right) \\ \frac{\partial C_j}{\partial T} = d_j \left( \frac{\partial^2 C_j}{\partial R^2} + \frac{\partial^2 C_j}{\partial Z^2} \right) \end{cases} \quad (22)$$

where  $C_j$  and  $d_j$  are the dimensionless concentration and the diffusion coefficient for species  $j$ .

In the same way, the dimensionless current responses for the four models are:

$$\begin{cases} J_S = -4\pi d_A \frac{\partial C_A}{\partial R} \big|_{R=1} \\ J_C = -2\pi L d_A \frac{\partial C_A}{\partial R} \big|_{R=1} \\ J_D = -2\pi d_A \int_0^1 \frac{\partial C_A}{\partial Z} \big|_{Z=0} R dR \\ J_B = -2L^* d_A \int_0^1 \frac{\partial C_A}{\partial Z} \big|_{Z=0} dR \end{cases} \quad (23)$$

where  $L$  and  $L^*$  are the dimensionless lengths for the cylinder and the band. Additionally, the parameter  $\alpha$  can be calculated using dimensionless current  $J$  and time  $T$ :

$$\alpha = 2 \frac{d(\log J)}{d(\log T)} + 1 \quad (24)$$

## 2.3 Computational methods

Simulation models were developed in *C++*, and the simulation results were processed via *Python* using the *NumPy* and *matplotlib* libraries. The diffusion equations were solved via matrices via the finite difference approach together with the alternating direction implicit (ADI) method [24–26]. Please refer to the textbook [23] for more details. Testing and validation [27–29] were performed including studies of error of mass conservation and convergence, which are shown in the Supplementary Information.

## 3 Theoretical analyses

In this section we summarise several literature analytical and empirical equations for the chronoamperometric responses, derive the parameter  $\alpha$  for microsphere, microcylinder, microdisc, and microband electrodes.

### 3.1 Microsphere electrode

The analytical expression of chronoamperometric current response of a

hemispherical electrode is [30]:

$$I = FADc^* \left( \frac{1}{\sqrt{D\pi t}} + \frac{1}{r_e} \right) \quad (25)$$

for which the dimensionless current  $J$  is:

$$J = 2\pi \left( \frac{1}{\sqrt{\pi T}} + 1 \right) \quad (26)$$

The expression for the diffusion indicator  $\alpha$  is:

$$\alpha = 2 \frac{d(\log J)}{d(\log T)} + 1 = 2T \frac{d(\ln J)}{dT} + 1 \quad (27)$$

Hence, combined with **Equation (26)**, the temporal evolution of  $\alpha$  for the hemispherical electrode can be expressed by:

$$\alpha = -\frac{1}{1+\sqrt{\pi T}} + 1 \quad (28)$$

### 3.2 Microdisc electrode

As reported by Shoup et al [17], an empirical expression for the chronoamperometric current response at a microdisc electrode based on fitting to simulations is:

$$I = 4Fr_e Dc^* \left\{ 0.7854 + 0.8863 \left( \frac{4Dt}{r_e^2} \right)^{-0.5} + 0.2146 \exp \left[ -0.7823 \left( \frac{4Dt}{r_e^2} \right)^{-0.5} \right] \right\} \quad (29)$$

where  $r_e$  is the disc radius. The error of this equation was reported [17] to be less than 0.6% for all times. In dimensionless form this becomes:

$$J = 3.1416 + 1.7726T^{-0.5} + 0.8584 \exp(-0.3912T^{-0.5}) \quad (30)$$

which, combined with **Equation (27)**, gives the temporal evolution of  $\alpha$  for the microdisc electrode:

$$\alpha = \frac{-1.7726T^{-0.5} + 0.3358T^{-0.5} \exp(-0.3912T^{-0.5})}{3.1416 + 1.7726T^{-0.5} + 0.8584 \exp(-0.3912T^{-0.5})} + 1 \quad (31)$$

### 3.3 Microcylinder electrode

The cylindrical electrode model discussed in this section refers to a cylinder with infinite length. Therefore, only the side of the cylinder is considered. As reported by Szabo et al [20], an empirical expression for the chronoamperometric current at a

microcylinder electrode of radius  $r_e$  is:

$$I = F D c^* l \left( \frac{e^{-0.1\sqrt{\pi T}}}{\sqrt{\pi T}} + \frac{1}{\ln[(4e^{-\gamma T})^{0.5} + e^{5/3}]} \right) \quad (32)$$

where  $\gamma$  is a constant which equals to 0.5772..., and the error of this equation was reported [20] to be less than 1.3% for all times. The dimensionless current  $J$  can be expressed as:

$$J = L \left( \frac{e^{-0.1\sqrt{\pi T}}}{\sqrt{\pi T}} + \frac{1}{\ln[(4e^{-\gamma T})^{0.5} + e^{5/3}]} \right) \quad (33)$$

which, combined with **Equation (27)**, give the temporal evolution of  $\alpha$  for the microband electrode:

$$\alpha = - \frac{\left( \frac{1}{10} + \frac{1}{\sqrt{\pi T}} \right) e^{-0.1\sqrt{\pi T}} + \frac{2\sqrt{T}e^{-0.5\gamma}}{(2\sqrt{T}e^{-0.5\gamma} + e^{5/3})[\ln(2\sqrt{T}e^{-0.5\gamma} + e^{5/3})]^2}}{\frac{e^{-0.1\sqrt{\pi T}}}{\sqrt{\pi T}} + \frac{1}{\ln(2\sqrt{T}e^{-0.5\gamma} + e^{5/3})}} + 1 \quad (34)$$

### 3.4 Microband electrode

In this section, the reference length is set to the width of the band  $w_e$  (rather than  $r_e$ ). As reported by Aoki et al. [31], an approximation for the chronoamperometric current of a microband electrode is:

$$I = F D c^* l \left[ \frac{1}{\sqrt{\pi T}} + 0.97 - 1.1 \exp\left(\frac{-9.9}{|\ln(12.37T)|}\right) \right] \quad (35)$$

where the error of this equation was reported [31] to be less than 0.8% for  $\log_{10} T \leq 8$ .

The dimensionless current  $J$  is:

$$J = L \left[ \frac{1}{\sqrt{\pi T}} + 0.97 - 1.1 \exp\left(\frac{-9.9}{|\ln(12.37T)|}\right) \right] \quad (36)$$

which, combined with **Equation (27)**, gives the temporal evolution of  $\alpha$  for the microband electrode:

$$\left\{ \begin{array}{l} \alpha = \frac{-\frac{1}{\sqrt{\pi T}} \pm \frac{21.78}{(\ln 12.37T)^2} \exp\left(\frac{-9.9}{|\ln(12.37T)|}\right)}{\frac{1}{\sqrt{\pi T}} + 0.97 - 1.1 \exp\left(\frac{-9.9}{|\ln(12.37T)|}\right)} + 1 \\ \pm \rightarrow \begin{cases} + & \text{when } \ln(12.37T) < 0 \\ - & \text{when } \ln(12.37T) \geq 0 \end{cases} \end{array} \right. \quad (37)$$

## 4 Results and discussion

The curves and trends for the currents and  $\alpha$  values are discussed in this section for the four electrodes with different geometries based on the literature analytical and empirical equations for their chronoamperometric current responses introduced in the previous section. Moreover, simulations for these four models are performed and concentration profiles are extracted at different timescales ( $\log_{10}T = -2, 0, 2, 4$ ) to obtain more information about the diffusion of the analyte  $A$  to the different electrode geometries. We note that in later sections we use the current densities to allow direct comparison between models. The dimensionless definitions of the current densities for the different models differ due to the differences in their geometries. The details are shown in **Table 2** where  $r_s$ ,  $r_d$  and  $r_c$  are the radii for the microsphere, microdisc and microcylinder, respectively,  $w$  is the dimensional width of microcylinder,  $l_c$  and  $l_b$  are the dimensional lengths for microcylinder and microband, respectively, and  $W$ ,  $L_c$  and  $L_b$  are their dimensionless counterparts.

**Table 2:** Dimensionless current densities for four different models

Model geometries	Microsphere	Microdisc	Microcylinder	Microband
Dimensional area (A)	$\frac{4}{3}\pi r_s^3$	$\pi r_d^2$	$2\pi r_c l_c$	$w l_b$
Dimensionless area (a)	$\frac{4}{3}\pi$	$\pi$	$2\pi L_c$	$L_b$
Current densities (J/a)	$\frac{3J}{4\pi}$	$\frac{J}{\pi}$	$\frac{3J}{4\pi}$	$\frac{3J}{4\pi}$

First, as shown in **Figure 4(A)**, the current responses normalised by the surface areas of different electrodes,  $J/a$  with  $\log_{10}-\log_{10}$  scales over a dimensionless time range from  $-6 \leq \log_{10}T \leq 6$ . When  $\log_{10}T < -2$ , the currents for all four electrodes follow the Cottrell equation. When  $\log_{10}T \geq -2$ , four currents start to deviate from the Cottrell equation, at different rates, approaching their steady- or quasi-steady states when  $\log_{10}T \geq 2$  as shown in the Supplementary Information. Specifically, as time continues, the steady-

state current density for the microdisc electrode is larger than that for the microsphere electrode. Similarly, the quasi-steady-state current density for the microband electrode is larger compared to that for the microcylinder electrode.

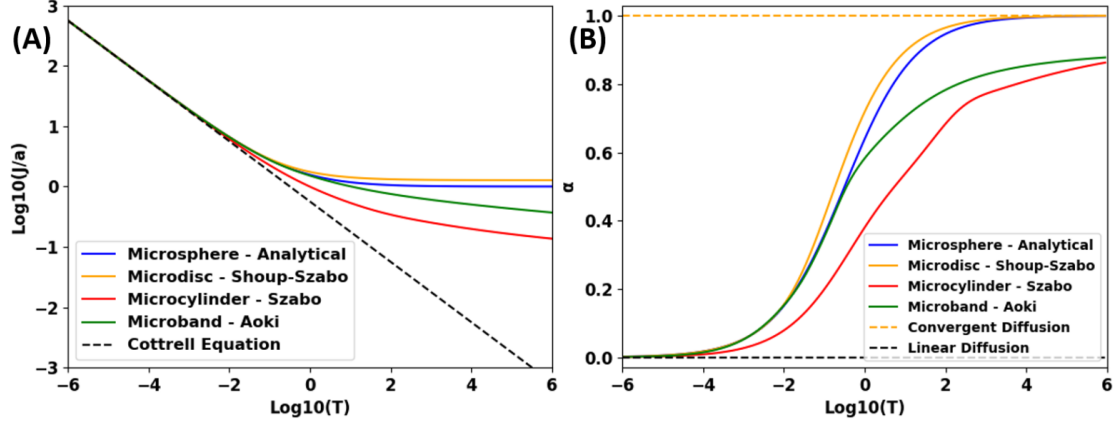


**Figure 4:** Temporal evolution of the current densities  $J/a$  (A) and  $\alpha$  values (B) for four different electrode geometries: microsphere (blue), microdisc (orange), microcylinder (red), microband (green). The limits of Cottrellian diffusion (linear diffusion, black), and convergent diffusion (yellow) are shown at  $\alpha = 0$  and 1, respectively.

Second, we present the temporal evolutions of the parameter  $\alpha$  in **Figure 4(B)** to obtain a straightforward, but sensitive illustration of the character of diffusion towards electrodes with different geometries. We see that the deviation from the linear, Cottrellian, diffusion starts even before  $\log_{10}T = -4$ . The  $\alpha$  values of the microdisc electrode and the microsphere electrode stay at closely similar values as that for the microband electrode until the  $\alpha$  value for the microdisc electrode start to approach the convergent diffusion limit faster than the other two electrodes at  $\log_{10}T = -2$ , and the  $\alpha$  value for the microsphere electrode starts to deviate from that for the microband electrode just after  $\log_{10}T = -1$ .

It is worth noting that the timescales for the  $\alpha$  values for the microdisc electrode and the microsphere electrode to reach the convergent diffusion limit are similar ( $\log_{10}T \approx 4$ ) despite the fact that the  $\alpha$  value for the microdisc electrode is generally larger than the  $\alpha$  value for the microsphere electrode over the range  $-2 \leq \log_{10}T \leq 4$ . We infer that

the edge diffusion at the microdisc electrode can be seen to give rise to a slightly more rapid response than the microsphere electrode. In contrast, the  $\alpha$  values for the microcylinder electrode and the microband electrode do not reach the convergent diffusion limit within the simulated period, reflecting the quasi-steady-state responses of these two electrodes. Larger  $\alpha$  values are noted for the microband electrode than the microcylinder electrode over the range  $-4 \leq \log_{10}T \leq 6$ , which can be explained by an analogous edge effect as inferred above.

In the following sections, using the concentration profiles at different timescales extracted from simulation results for the four electrode models, we comparatively discuss the character of the diffusion on the  $\alpha$  value.

#### 4.1 Microsphere and microcylinder electrodes

The concentration profiles near the electrode surfaces for the microsphere and the microcylinder electrodes are shown in **Figure 5(A-D)** and **5(E-H)**, respectively, at  $\log_{10}T = -2, 0, 2, 4$ . The plots take the form of dimensionless concentration as a function of the dimensionless radial coordinate  $R$ . **Figure 5(A)** and **5(E)** show that the depleted area of the analyte  $A$  around the electrode surface for the microcylinder electrode is obviously larger than that for the microsphere electrode at  $\log_{10}T = -2$ . As time evolves, the depleted areas increase for both models, and the depleted area for the microcylinder electrode stays larger than that for the microsphere electrode across the entire timescale shown in **Figure 5**.

Based on these findings, together with the fact that, after  $\log_{10}T = -4$ , the current density and the  $\alpha$  values for the microsphere electrode are larger than those for the microcylinder electrode once they start to deviate from the Cottrell equation, as shown in **Figure 4**, we can assert that there is a huge difference in the diffusion towards these two electrodes as soon as their current responses deviate from the Cottrell equation.

This is due to the three-dimensional radial diffusion from/to the microsphere electrode resulting in a larger diffusion source, and hence larger current density and  $\alpha$  values. In contrast the two- dimensional radial diffusion from/to the microcylinder electrode is less effective.

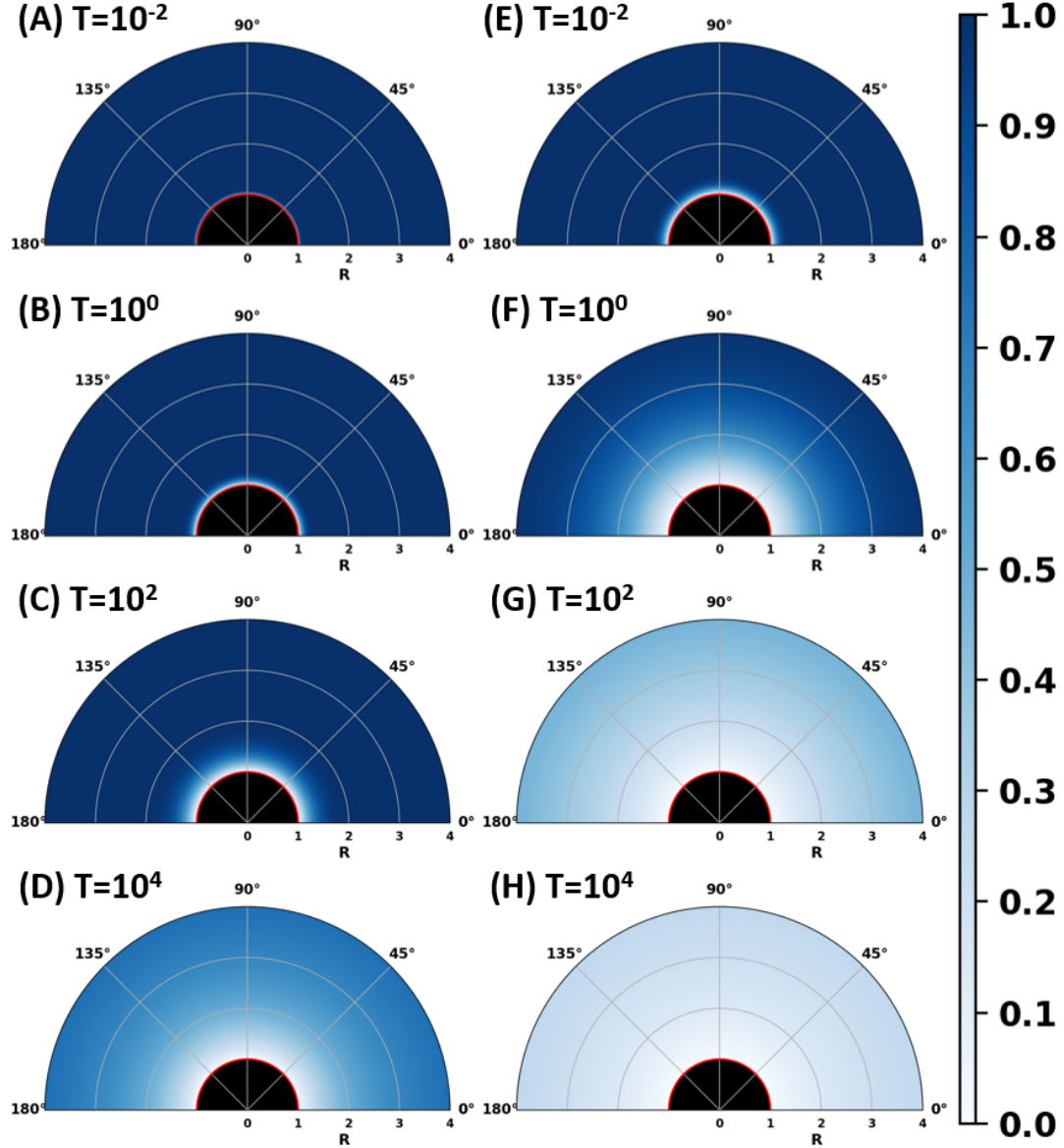


**Figure 5:** Concentration profiles extracted for the microsphere electrode (A-D) and the microcylinder electrode (E-H) at  $\log_{10} T = -2, 0, 2, 4$  from top to bottom.

## 4.2 Microdisc and microband electrodes

The concentration profiles, in  $(R, Z)$  space, near the electrode surfaces for the microdisc and the microband electrodes are shown in **Figure 6(A-D)** and **6(E-H)**,

respectively, at  $\log_{10} T = -2, 0, 2, 4$ . As shown in **Figure 6(A)** and **6(E)**, the depleted areas of the analyte  $A$  around the electrode surfaces for the microdisc electrode and the microband electrode are almost identical at  $\log_{10} T = -2$ . As time evolves, however, the depleted areas increase for both models, but the depleted area for the microcylinder electrode grows faster than that for the microdisc electrode shown in **Figure 6**.

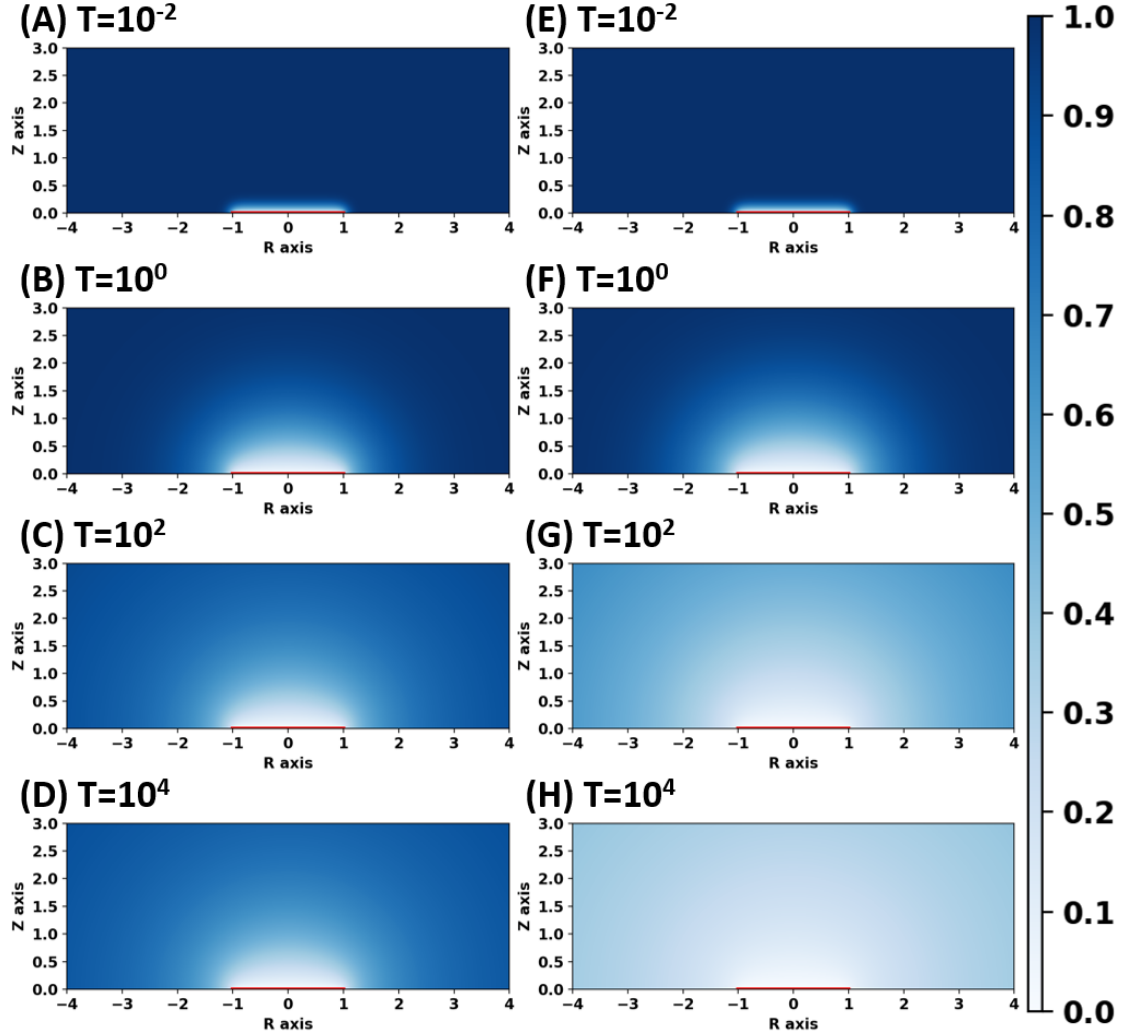


**Figure 6:** Concentration profiles extracted for the microdisc electrode (A-D) and the microband electrode (E-H) at  $\log_{10} T = -2, 0, 2, 4$  from top to bottom.

These findings echo the curves for the currents and  $\alpha$  values for these two electrodes in **Figure 4**. At  $\log_{10} T = -2$ , there is no obvious difference in the plots of currents and  $\alpha$  values. For  $\log_{10} T > -2$ , the  $\alpha$  values for the microband increases less rapidly than that for the microdisc electrode. This is caused by the additional radial diffusion for the

microdisc electrode.

To help clarify the apparent contradictory observations namely that the depletion rate of the microsphere electrode is slower than the microdisc electrode at  $0 \leq \log_{10}T \leq 2$  while the  $\alpha$  values for the microsphere electrode is smaller than those for the microdisc electrode in this interval, we note here the direct comparison in terms of the depleted areas is not recommended under different simulation coordinates due to following reasons:

First, in **Figure 5**, we presented the areas  $\Delta R = 3$  beyond the electrode surface, while it is shown in **Figure 6**  $\Delta R = 3$  and  $\Delta Z = 3$  beyond the electrode surface, which already results in intrinsic differences between concentration profiles and difficulties in comparison between different coordinate systems. Thus, the concentration profiles for different coordinate systems are not able to illustrate the fact that the edge effect for the microdisc electrode offers larger diffusive flux, though the apparent depletion rate for the microsphere electrode is slow.

Second, the difference in coordinate systems between the microsphere electrode and microdisc electrode will directly influence the depleted areas shown. The fact that the edge effect for the microdisc electrode allows its  $\alpha$  values to be higher than those for the microsphere electrode at  $0 \leq \log_{10}T \leq 2$ , meanwhile, increases the shown depleted areas because of a weaker planar diffusive flux and a depleted edge side area.

## 5 Conclusions

We have introduced a new parameter, the diffusion indicator  $\alpha$  and applied this parameter to derive expressions for  $\alpha$  from literature analytical and empirical equations for four different electrode geometries. Comparison of the current densities and the  $\alpha$  values between the selected electrodes with the help of concentration profiles extracted from the simulations showed the different contributions of planar and convergent

diffusion in the different geometries. This newly introduced parameter  $\alpha$  has a high sensitivity when investigating the diffusion phenomena whilst is simple and straightforward to use and analyse.

## References

- [1] L. Bieniasz, J. González, Á. Molina, E. Laborda, *Electrochimica Acta*, **2010**, *56*, 543–552.
- [2] Y. Liu, H. Cai, H. Li, *Journal of Manufacturing Processes*, **2015**, *17*, 162–170.
- [3] S. Li, C. Peng, Y. Liu, K. Wang, H. Kong, Z. Wei, *The International Journal of Advanced Manufacturing Technology*, **2019**, 1–9.
- [4] I. B. Svir, A. I. Oleinick, *Journal of Electroanalytical Chemistry*, **2001**, *499*, 30–38.
- [5] S. Eloul, R. G. Compton, *ChemElectroChem*, **2014**, *1*, 917–924.
- [6] S. Eloul, E. Kätelhön, C. Batchelor-McAuley, K. Tschulik, R. G. Compton, *Journal of Electroanalytical Chemistry*, **2015**, *755*, 136–142.
- [7] K. Ngamchuea, C. Lin, C. Batchelor-McAuley, R. G. Compton, *Analytical Chemistry*, **2017**, *89*, 3780–3786.
- [8] L. Chen, C. Lin, R. G. Compton, *Phys. Chem. Chem. Phys.*, **2018**, *20*, 15795–15806.
- [9] C. Zhang, N. Driver, Q. Tian, W. Jiang, H. Liu, *Journal of Biomedical Materials Research - Part A*, **2018**, *106*, 1887–1895.
- [10] D. Li, C. Batchelor-McAuley, L. Chen, R. G. Compton, *Phys. Chem. Chem. Phys.*, **2019**, *21*, 9969–9974.
- [11] D. H. Craston, C. P. Jones, D. E. Williams, N. E. Murr, *Talanta*, **1991**, *38*, 17–26.
- [12] J. A. Alden, R. G. Compton, *Journal of Electroanalytical Chemistry*, **1996**, *404*, 27–35.
- [13] L. Authier, C. Grossiord, P. Brossier, B. Limoges, *Analytical Chemistry*, **2001**, *73*, 4450–4456.
- [14] C. Amatore, E. Maisonhaute, G. Simonneau, *Electrochemistry Communications*, **2000**, *2*, 81–84.
- [15] C. Amatore, E. Maisonhaute, G. Simonneau, *Journal of Electroanalytical Chemistry*, **2000**, *486*, 141–155.
- [16] K. Aoki, J. Osteryoung, *Journal of Electroanalytical Chemistry*, **1981**, *122*, 19–35.
- [17] D. Shoup, A. Szabo, *Journal of Electroanalytical Chemistry*, **1982**, *140*, 237–245.
- [18] S. Coen, D. K. Cope, D. E. Tallman, *Journal of Electroanalytical Chemistry*, **1986**, *215*, 29–48.
- [19] P. M. Kovach, W. L. Caudill, D. G. Peters, R. M. Wightman, *Journal of Electroanalytical Chemistry*, **1985**, *185*, 285–295.
- [20] A. Szabo, D. K. Cope, D. E. Tallman, P. M. Kovach, R. M. Wightman, *Journal of Electroanalytical Chemistry*, **1987**, *217*, 417–423.
- [21] H. Le, E. Kätelhön, R. G. Compton, *Journal of Electroanalytical Chemistry*, **2019**, *855*, 113602.
- [22] I. B. Svir, A. I. Oleinick, R. G. Compton, *Russian Journal of Electrochemistry*, **2003**, *39*, 160–164.
- [23] R. G. Compton, E. Laborda, K. R. Ward, *Understanding Voltammetry: Simulation of Electrode Processes*, Imperial College Press, **2013**.

- [24] D. Peaceman, H. Rachford, Jr., *Journal of the Society for Industrial and Applied Mathematics*, **1955**, 3, 28–41.
- [25] J. Heinze, *Journal of Electroanalytical Chemistry and Interfacial Electrochemistry*, **1981**, 124, 73–86.
- [26] J. A. Alden, R. G. Compton, *The Journal of Physical Chemistry B*, **1997**, 101, 8941–8954.
- [27] E. Kätelhön, R. G. Compton, *Analyst*, **2015**, 140, 2592–2598.
- [28] E. Kätelhön, R. G. Compton, *Analyst*, **2015**, 140, 3290–3290.
- [29] E. Kätelhön, R. G. Compton, *Analyst*, **2016**, 141, 1154–1154.
- [30] R. G. Compton, C. E. Banks, *Understanding Voltammetry*, Third, World Scientific Press, **2018**.
- [31] K. Aoki, K. Tokuda, H. Matsuda, *Journal of Electroanalytical Chemistry*, **1987**, 230, 61–67.